Nanoscale

COMMUNICATION

View Article Online
View Journal | View Issue

Cite this: *Nanoscale*, 2023, **15**, 483

Received 14th October 2022,
Accepted 8th December 2022

DOI: 10.1039/d2nr05705k

rsc.li/nanoscale

New horizons of MBenes: highly active catalysts for the CO oxidation reaction†

Bikun Zhang,[a,b] Jian Zhou *[a,b] and Zhimei Sun *[a,b]

The search for materials with high intrinsic carbon monoxide oxidation reaction (COOR) catalytic activity is critical for enhancing the efficiency of reducing CO contamination. COOR catalysts, however, have long relied heavily on noble metals and CeO_2. Herein, in order to search for non-noble COOR catalysts that are more active than CeO_2, 18 oxygen-functionalized MBenes with orthorhombic and hexagonal crystal structures, denoted as orth-$M_2B_2O_2$ and hex-$M_2B_2O_2$ (M = Ti, V, Cr, Zr, Nb, Mo, Hf, Ta and W), were investigated in terms of their COOR catalytic activity by high-throughput first-principles calculations. Hex-$Mo_2B_2O_2$, orth-$Mo_2B_2O_2$, hex-$V_2B_2O_2$ and hex-$Cr_2B_2O_2$ were found to be more active than CeO_2 and possess structural stability below 1000 K, showing the potential to replace CeO_2 as the substrates of COOR catalysts. Moreover, orth-$Mo_2B_2O_2$, hex-$V_2B_2O_2$ and hex-$Cr_2B_2O_2$ exhibit even higher COOR catalytic activity than Pt–CeO_2 and Au–CeO_2, and are expected to be applied as COOR catalysts directly. Further investigations showed that the formation energy of oxygen vacancies could be used as the descriptor of COOR catalytic activity, which would help to reduce the amount of calculations significantly during the catalyst screening process. This work not only reports a series of 2D materials with high COOR catalytic activity and opens up a new application area for MBenes, but also provides a reliable strategy for highly efficient screening for COOR catalysts.

Introduction

Carbon monoxide (CO) is one of the major air pollutants and is not only toxic to human beings, but also results in the poisoning of Pt-based catalysts in proton-exchange membrane fuel cells (PEMFC).[1,2] CO originates mostly from the exhaust gas of internal combustion engines,[3] and one of the most common methods for CO treatment is the carbon monoxide oxidation reaction (COOR), in which CO is oxidized to carbon dioxide (CO_2) at low temperature in an O_2 atmosphere without combustion.[4–7] There exist three typical mechanisms for COOR catalysis: the Langmuir–Hinshelwood (L–H) mechanism, the Eley–Rideal (E–R) mechanism and the Mars–van Krevelen (M–vK) mechanism.[3] In the L–H and E–R mechanisms, all the CO molecules are oxidized by O_2 molecules and the lattices of catalysts remain intact during the whole catalytic process. As illustrated in Scheme 1, in the L–H mechanism, the catalysts adsorb both CO and O_2 molecules, while in the E–R mechanism, the catalysts only adsorb O_2 molecules. However, in the M–vK mechanism, the CO molecules are oxidized by both O_2 molecules and the lattice oxygen atoms on the surfaces of the catalysts, which means that the catalysts are involved in the elementary reactions directly. During the catalytic process, oxygen vacancies (Va_O) are generated when the lattice oxygen atoms are used to oxidize CO molecules, and they will be filled with O_2 molecules in the next elementary step.[8,9] In general, on catalysts with metal active sites (including single atoms, clusters and nanoparticles) and inert substrates (such as graphene[7]), the COOR occurs *via* the L–H and E–R mechanisms, while only on catalysts containing accessible lattice oxygen atoms could the COOR occur *via* the M–vK mechanism.

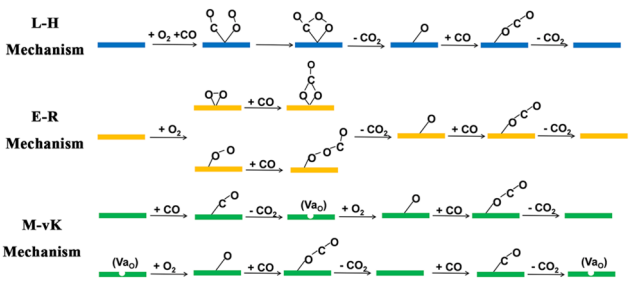

Scheme 1 Three different mechanisms of COOR catalysis.

[a]*School of Materials Science and Engineering, Beihang University, Beijing 100191, China. E-mail: jzhou@buaa.edu.cn, zmsun@buaa.edu.cn*
[b]*Center for Integrated Computational Materials Engineering, International Research Institute for Multidisciplinary Science, Beihang University, Beijing 100191, China*
† Electronic supplementary information (ESI) available. See DOI: https://doi.org/10.1039/d2nr05705k

So far, noble metals, such as Pt, Pd, and Au, are indispensable for most COOR catalysts. To reduce the use of noble metals and control the cost, one popular strategy is to load single atoms or nanoparticles of noble metals or their oxides on non-noble substrates, such as Pt/CeO_2, Pd/CeO_2 and Au/CeO_2,[5,8–23] which have been universally adopted in three-way catalytic converters (TWCs) in the exhaust systems of vehicles to remove CO, which is one of the major harmful gases. The most commonly used COOR catalysts is CeO_2-supported noble metals because the lattice oxygen atoms in CeO_2 could be easily utilized, making the COOR occur *via* the M–vK mechanism with high activity.[8,11,14,15,19,24–26] The intrinsic catalytic activity of substrates contributes a lot to the overall performance of COOR catalysts since the substrates are involved in the oxidation of CO directly *via* the M–vK mechanism. However, the intrinsic catalytic activity of CeO_2 is relatively poor.[3] Therefore, the search for materials with higher intrinsic COOR catalytic activity to replace CeO_2 will be beneficial for enhancing the COOR catalytic performance of combined catalysts.

Lattice oxygen atoms are indispensable to the intrinsic COOR catalytic activity of non-noble catalysts.[3,27] In the past decade, two-dimensional transition metal carbides/nitrides/carbonitrides, MXenes, have been widely studied as catalysts for various reactions. The exposed transition metal atoms on the surfaces of MXenes are easily functionalized by oxygen atoms which can tune their properties.[28–30] According to the previous research by Tahini *et al.*,[27] the interaction between the transition metal atoms and the surface oxygen atoms in $Cr_3C_2O_2$, $V_3C_2O_2$ and $Sc_3C_2O_2$ MXenes is relatively weak, and thus the surface oxygen atoms could be easily utilized to oxidize CO molecules. By studying the COOR catalytic activity, it was found that these O-functionalized MXenes are more active than CeO_2 *via* the M–vK mechanism. In 2017, MBenes, a family of two-dimensional transition metal borides, were reported,[31] and they possess similar structures to MXenes.[32] MBenes are widely studied as catalysts or substrates of various reactions, including the hydrogen evolution reaction (HER),[31,33–36] the oxygen evolution reaction (OER)/oxygen reduction reaction (ORR),[34,37] the nitrogen reduction reaction (NRR)[38–40] and the CO_2 reduction reaction (CO_2RR).[41,42] Similar to the situation for MXenes, the exposed transition metal surfaces of pristine MBenes can be easily functionalized by O atoms.[35,37,43,44] Therefore, it is anticipated that the surface oxygen atoms on O-functionalized MBenes could also be utilized to oxidize CO molecules leading to high COOR catalytic activity *via* the M–vK mechanism.

In this work, 18 O-functionalized MBenes, denoted as orth-$M_2B_2O_2$ and hex-$M_2B_2O_2$, where M represents Ti, V, Cr, Zr, Nb, Mo, Hf, Ta, and W, and "orth/hex" indicates orthorhombic/hexagonal crystal systems, were investigated to explore their intrinsic COOR catalytic activity and mechanism by means of the first-principles method. Our calculated results show that five $M_2B_2O_2$ compounds demonstrate higher COOR catalytic activity than CeO_2 at room temperature and good thermal stability at a high temperature of 1000 K, among which, orth-$Mo_2B_2O_2$, orth-$W_2B_2O_2$, hex-$V_2B_2O_2$ and hex-$Cr_2B_2O_2$ are eligible to serve as independent COOR catalysts. Moreover, it has been found that oxygen vacancy formation energy could reflect the maximum reaction energy for the COOR directly. Therefore, by taking oxygen vacancy formation energy as the descriptor for COOR catalytic activity, the screening efficiency for COOR catalysts could be highly improved.

Computational methods

All first-principles calculations were performed based on density functional theory (DFT) using the Vienna *ab initio* Simulation Package (VASP)[45,46] with the projector-augmented wave (PAW) method.[47] The interaction between ion cores and valence electrons was described using the Perdew–Burke–Ernzerhof (PBE) functional.[48,49] All the atomic structures were fully relaxed under the energy and force convergence criteria of 10^{-4} eV per atom and 0.02 eV per angstrom, respectively. For the calculation of energy, $3 \times 3 \times 1$ supercells were used, while for *ab initio* molecular dynamics (AIMD) simulation, $4 \times 4 \times 1$ supercells were applied, during which a canonical *NVT* ensemble was used, and the temperature was controlled with the algorithm of Nosé.[50]

In this work, COOR catalysis on 18 orth/hex-$M_2B_2O_2$ *via* the M–vK mechanism was studied, which involves three phases: the adsorption of O_2 (I:* + O_2 → *OO), the formation of the first CO_2 (II: *OO + CO → *OOCO and III: *OOCO → CO_2 + *O) and the formation of the second CO_2 (IV: *O + CO → *CO_2 and V: *CO_2 → * + CO_2). Here * represents $M_2B_2O_2$ with O vacancies. The Gibbs free energy of steps I∼V is denoted as $\Delta G_1 \sim \Delta G_5$. The computational details of the energy terms are included in the ESI.†

Results and discussion

The 18 orth/hex-M_2B_2 compounds studied in this work have been proved to be stable dynamically according to the previous research studies.[31–33,37,51–55] Experimentally, oxygen functional groups have been detected on the surface of hex-$Mo_{4/3}B_2$ MBenes.[56] Meanwhile, theoretical studies of O-functionalized MBenes have been carried out in many studies.[31,35,36,43,54,57,58] First of all, we studied the atomic structures of 18 $M_2B_2O_2$ and the corresponding formation energy of oxygen functional groups. There exist four and two sites with different chemical environments for O atoms binding on the surfaces of orth-M_2B_2 and hex-M_2B_2, respectively (Fig. S1(a) and S2(a)†). Considering the symmetry of orth-M_2B_2 and hex-M_2B_2, we investigated four types of atomic structures for orth-M_2B_2, including types I–III shown in Fig. 1(a–c) and type IV shown in Fig. S1(b),† and three types of atomic structures for hex-M_2B_2, including types A and B shown in Fig. 1(d and e) and type C shown in Fig. S2(b).† After studying the total energy of all the structures of the 18 $M_2B_2O_2$, the most stable structures for each are shown in Fig. 1. There are three types of atomic structures for orth-$M_2B_2O_2$: type-I for M = Ti, Zr, Hf, Mo; type-II for

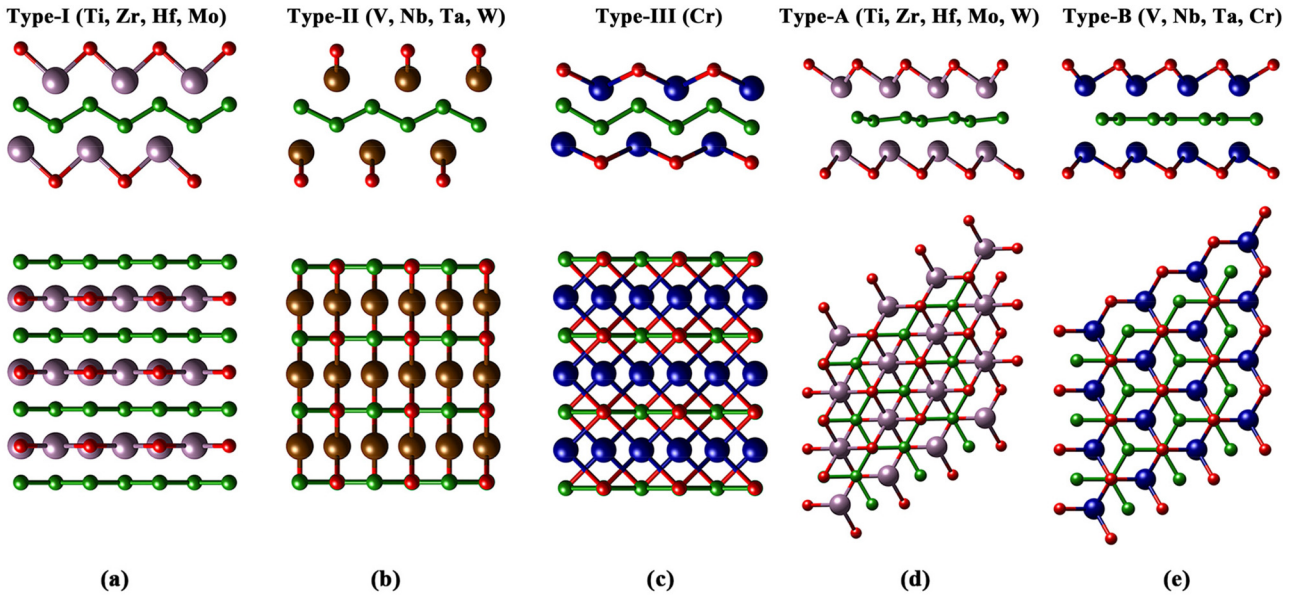

Fig. 1 The optimized atomic structures of (a) type-I, (b) type-II, (c) type-III for orth-$M_2B_2O_2$ and (d) type-A, (e) type-B for hex-$M_2B_2O_2$ in side (up) and top (down) views. Green and red balls represent B and O atoms, respectively, and the balls with other colors represent transition metal atoms.

M = V, Nb, Ta, W; and type-III for M = Cr, while there are two different atomic structures for hex-$M_2B_2O_2$: type-A for M = Ti, Zr, Hf, Mo, W and type-B for M = V, Nb, Ta, Cr. For the most stable structure for each $M_2B_2O_2$, the formation energy of the oxygen functional group (ΔG_f^O) was calculated with eqn (S4),† and the results are listed in Table S2.† For all 18 $M_2B_2O_2$, the values of ΔG_f^O are negative, indicating the spontaneity of the formation of oxygen functional groups under an O_2 atmosphere thermodynamically. These surface oxygen atoms could serve as the oxidants of CO molecules in COOR catalysis.

In general, the surface vacancies on O-functionalized MXenes are inevitable.[28,59] Therefore, we considered the existence of oxygen vacancies on the surface of $M_2B_2O_2$ in this work. Here the concentration of O vacancies is considered to be 5.56%, corresponding to one O vacancy in a 3 × 3 × 1 supercell of $M_2B_2O_2$. The formation energy of oxygen vacancies, ΔG_f^{Va}, was calculated with eqn (S5)† and the results are listed in Table S2.† The results show that the values of ΔG_f^{Va} for the 18 $M_2B_2O_2$ range from 2.55 eV to 5.59 eV. In addition, the values of ΔG_f^{Va} for two O-functionalized MXenes, Ti_2CO_2 and $Ti_3C_2O_2$, were calculated to be 4.5 eV and 5.0 eV (the concentration of O vacancies = 5.56%), respectively, which are higher than those of most of the $M_2B_2O_2$, as displayed in Fig. 2. Since O vacancies on Ti_2CO_2 and $Ti_3C_2O_2$ are very common in experiments,[28,60] the $M_2B_2O_2$ studied here can also easily become defective with O vacancies, which could capture CO molecules.

From Fig. 2, it is found that for orth/hex-$M_2B_2O_2$ with M in the same group, the ΔG_f^{Va} values increase with increasing atomic number (Z), while for $M_2B_2O_2$ with M in the same period, the ΔG_f^{Va} values decrease with increasing electron layer number (n). Therefore, orth/hex-$Cr_2B_2O_2$ has the lowest ΔG_f^{Va}

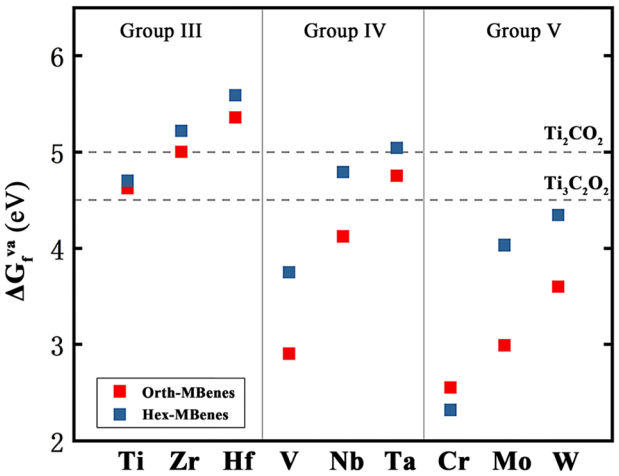

Fig. 2 The formation energy of oxygen vacancies of 18 $M_2B_2O_2$, in comparison with those of Ti_2CO_2 and $Ti_3C_2O_2$.

value, while orth/hex-$Hf_2B_2O_2$ has the highest ΔG_f^{Va} value. Apparently, the variation of ΔG_f^{Va} is in accordance with the periodic law of elements: the larger Z and the lower n M has, the lower ΔG_f^{Va} value $M_2B_2O_2$ has.

The electrons on the surfaces of defective $M_2B_2O_2$ are not evenly distributed due to the existence of O vacancies, which are easy to fill with gaseous molecules. According to the results of Bader charge calculations, the transition metal atoms nearest to the O vacancies have lower coordination number than the other transition metal atoms, and thus they possess more electrons. The extra electrons could transfer to the 2p orbitals of the O atoms in O_2 or CO molecules to drive

the electron distribution of the transition metal layers equally. Theoretically, both O_2 and CO molecules could adsorb at the O vacancy sites. However, if CO molecules fill the O vacancies, the C atoms would be left on the surface, which could not be removed by combining with O_2 to form CO_2. This would result in the blockage of O_2 adsorption sites and deactivation of the catalysts. Therefore, we investigated the adsorption selectivity of O vacancies by calculating the adsorption energy of O_2 and CO, as shown in Fig. 3(a). Apparently, the adsorption of O_2 on all 18 defective $M_2B_2O_2$ is highly spontaneous with the O_2 adsorption energy being lower than −1 eV, while the values of CO adsorption energy are all higher than 0. Taking orth-$Cr_2B_2O_2$ and hex-$Cr_2B_2O_2$ as examples, after adsorbing CO, the O atoms of CO could not fill the O vacancies and the CO molecules would stay above the surfaces, as displayed in Fig. S3(a and b).† Therefore, all 18 defective $M_2B_2O_2$ compounds have higher adsorption selectivity towards O_2 than towards CO, avoiding the deactivation of catalysts.

As shown in Fig. 3(b), an O_2 molecule adsorbs on the O vacancy site perpendicularly to the surfaces of most $M_2B_2O_2$. However, for orth-$Ta_2B_2O_2$ and hex-$Zr_2B_2O_2$, O_2 molecules are parallel with the surfaces (Fig. S3(c and d)†), while for hex-$Hf_2B_2O_2$, after the vacancy is filled with one O atom of O_2, the other O atom adsorbs on the top of the Hf atom (Fig. S3(e)†). To study the mechanism, we further calculated the change in the O–O bond length (Δd) and the number of electrons that the O_2 molecules obtain from the substrates (N_e), which are listed in Table S3.† The O–O bond length of O_2 increases on all 18 $M_2B_2O_2$ after adsorption, indicating that the O_2 molecules are activated by $M_2B_2O_2$ and the O–O bonds become weaker. By analyzing the relationship between Δd and N_e, it is found from Fig. 3(c) that Δd is approximately proportional to N_e, implying that the more electrons the O_2 molecules obtain, the stronger the O_2 activation degree is, contributing to a longer O–O bond.

After the adsorption of O_2, the outer O atom combines with the gaseous CO molecule, thus forming the OOCO intermediates (step II). This step is highly spontaneous for all 18 $M_2B_2O_2$ compounds, with ΔG_2 ranging from −4 eV to −6 eV. It is notable that the OOCO intermediates exist as separate adsorbed O and isolated OCO from the $M_2B_2O_2$ substrates, as illustrated in Fig. 4(a). The isolated OCO is located at a distance of over 2.8 Å above the surfaces of $M_2B_2O_2$, which suggests that the binding strength between the $M_2B_2O_2$ substrates and the outer O atom is extremely weak. Consequently, it is very easy for the outer O atoms to detach from the substrates and combine with the CO molecules, which is attributed to the O_2 activation by substrates. Further study of Bader charge indicated that there is barely electron transfer between the substrates and OCO. In other words, no chemisorption exists between the two moieties and the binding strength is relatively low. Therefore, step III is also exothermic, generating gaseous CO_2 molecules with ΔG_3 ranging from 0 to −0.5 eV. The values of Gibbs free energy change for the formation of the first CO_2 ($\Delta G_2 + \Delta G_3$) are listed in Table S4.†

After desorption of the first CO_2, the surfaces of substrates become complete and flat, and all the O atoms could serve as the adsorption sites for CO molecules. During this process, the values of ΔG_4 are negative for orth-$V_2B_2O_2$ (−0.59 eV), orth-$Cr_2B_2O_2$ (−0.56 eV), orth-$Mo_2B_2O_2$ (−0.60 eV) and hex-$Cr_2B_2O_2$ (−0.87 eV). For these materials, the subsequent CO_2 desorption process requires more energy input with ΔG_5 ranging from −0.28 eV to 0.1 eV, and thus ΔG_5 is the maximum Gibbs free energy change (ΔG_{max}) for the whole COOR. For the other $M_2B_2O_2$ compounds, the adsorption of the second CO molecules is endothermic and the most energy-consuming step, among which orth-$Nb_2B_2O_2$, orth-$W_2B_2O_2$, hex-$V_2B_2O_2$ and hex-$Mo_2B_2O_2$ have ΔG_{max} lower than 1 eV. The values of ΔG_4 and ΔG_5 for all 18 $M_2B_2O_2$ are listed in Table S5.† Besides, the COOR catalytic activity of CeO_2 was also studied. The supercell of CeO_2 contains 18 surface O atoms, which is the same as for the $M_2B_2O_2$ studied in this work, and the ΔG_{max} for CeO_2 is calculated to be 0.93 eV. It was found that the features in terms of reaction energy are similar for CeO_2 and $M_2B_2O_2$: easy adsorption of O_2, easy formation of the first CO_2, but hard for-

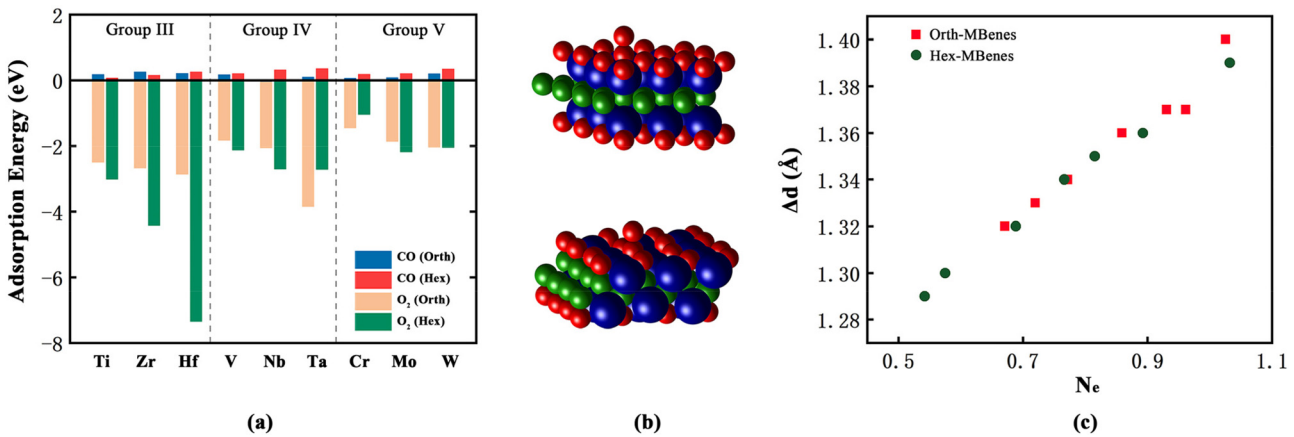

Fig. 3 (a) The adsorption energy of O_2 and CO on 18 defective $M_2B_2O_2$. (b)The structures after O_2 adsorption on hex-$Cr_2B_2O_2$ (up) and orth-$Cr_2B_2O_2$ (down). Blue, green and red balls represent transition metal, B and O atoms, respectively. (c) The relationship between the O–O bond length (Δd) and the numbers of electrons that the O_2 molecules obtains from the substrates (N_e).

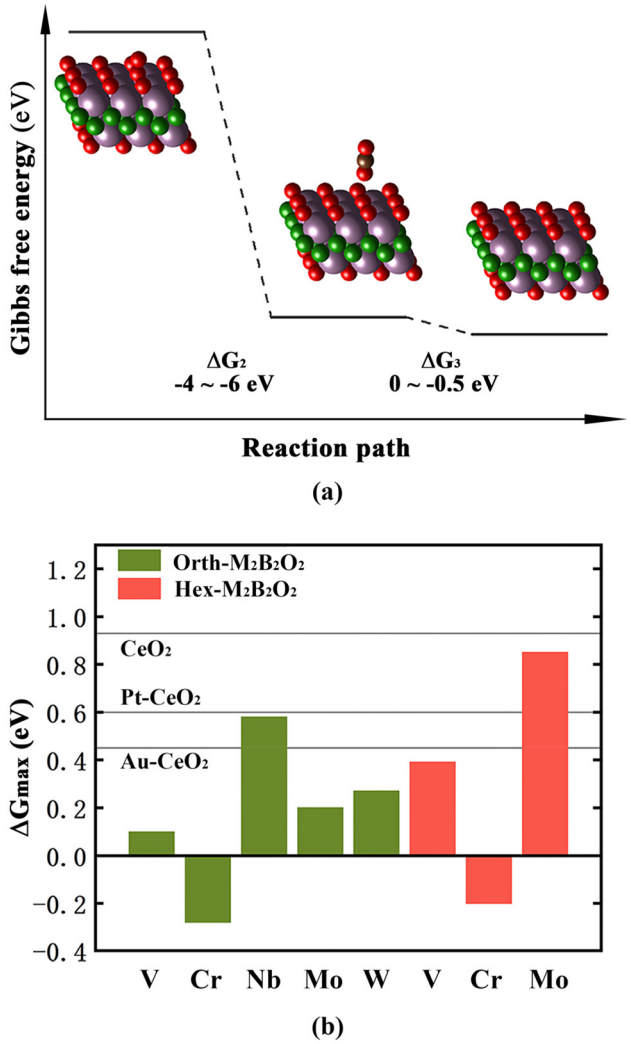

Fig. 4 (a) Gibbs free energy profile for steps II and III. (b) ΔG_{max} for COOR of orth-$V_2B_2O_2$, orth-$Cr_2B_2O_2$, orth-$Nb_2B_2O_2$, orth-$Mo_2B_2O_2$, orth-$W_2B_2O_2$, hex-$V_2B_2O_2$, hex-$Cr_2B_2O_2$, hex-$Mo_2B_2O_2$, compared with CeO_2, Pt–CeO_2 and Au–CeO_2.

mation of the second CO_2. As shown in Fig. 4(b), the eight $M_2B_2O_2$ mentioned above are more active than CeO_2 for COOR catalysis. Moreover, except hex-$Mo_2B_2O_2$, these $M_2B_2O_2$ compounds possess COOR catalytic activities even higher than those of CeO_2-based single atom catalysts, Pt–CeO_2 and Au–CeO_2 (ΔG_{max} = 0.60 eV and 0.45 eV, respectively), which have been considered as highly active COOR catalysts experimentally according to the previous studies.[11,26] Since the COOR is widely used for CO removal in exhaust gas, the catalysts should maintain the stability of their structures at high temperature. By *ab initio* molecular dynamics (AIMD) simulation at 1000 K for 10 ps, hex-$Mo_2B_2O_2$, orth-$Mo_2B_2O_2$, hex-$V_2B_2O_2$ and hex-$Cr_2B_2O_2$ were found to be stable with tiny energy fluctuation and structural distortion, as seen in Fig. S4.† Therefore, we conclude that hex-$Mo_2B_2O_2$, orth-$Mo_2B_2O_2$, hex-$V_2B_2O_2$ and hex-$Cr_2B_2O_2$ could all serve as the substitutes for CeO_2 as the substrates of COOR catalysts. Furthermore, orth-$Mo_2B_2O_2$, hex-$V_2B_2O_2$ and hex-$Cr_2B_2O_2$ are expected to be used as COOR catalysts directly.

As the COOR catalysis involves five elementary steps, it is very time-consuming to calculate the Gibbs free energy changes for all the elementary steps to screen the desired COOR catalysts from many candidates. Therefore, to simplify the screening process and reduce the amount of calculations, here we tried to find out a general descriptor for the COOR catalytic activity by investigating the relationship between ΔG_{max} of $M_2B_2O_2$ and species of M. In Fig. 5(a and b) the ΔG_{max} values of orth-$M_2B_2O_2$ and hex-$M_2B_2O_2$ are shown in the form of a three-dimensional bar graph. It can be seen that the values of ΔG_{max} vary with the species of transition metal elements, in line with the periodic law of elements: for M in the same period, ΔG_{max} of $M_2B_2O_2$ decreases with increasing atomic number (Z), while for M in the same group, ΔG_{max} of $M_2B_2O_2$ becomes higher with increasing electron layer number (n). Therefore, orth/hex-$Cr_2B_2O_2$ has the smallest ΔG_{max} while orth/hex-$Hf_2B_2O_2$ has the largest ΔG_{max}.

As discussed above, the periodic law of elements was also found in the variation of ΔG_f^{Va} with species of M. Therefore, we correlate ΔG_{max} with ΔG_f^{Va}, and the results are demonstrated in Fig. 5(c). The data dots in the figure indicate that there exists close correlation between ΔG_{max} and ΔG_f^{Va}. By linearly fitting the dot data, it is found that the determination coefficient, *i.e.*, R^2, reached 0.94, indicating the high degree of linear relationship between the two parameters. Meanwhile, the ΔG_f^{Va} value of CeO_2 with an O vacancy density of 5.56% was calculated to be 3.94 eV. The coordinates (ΔG_f^{Va}, ΔG_{max}) for CeO_2 are indicated with the blue star in Fig. 5(c), which is clearly very close to the fitted line. Therefore, the oxygen vacancy formation energy can directly reflect the COOR catalytic activity of materials. Generally, the lower the ΔG_f^{Va}, the lower the ΔG_{max}, which implies higher COOR catalytic activity.

By using ΔG_f^{Va} as the descriptor for the COOR catalytic activity, the screening of COOR catalysts with high activity will become much easier because only the values of ΔG_f^{Va} need to be calculated while the time-consuming calculations of ΔG for all the elementary steps are unnecessary. Subsequently, the investigation of the COOR catalytic activity of 9 M_2CO_2 MXenes was conducted, where M represents the same transition metal atoms as those of $M_2B_2O_2$ in this work. Here, we calculated the ΔG_f^{Va} of the 9 M_2CO_2 first, which shows the periodic variation with M, the same as in the case of $M_2B_2O_2$. Among the 9 M_2CO_2, only Cr_2CO_2 and V_2CO_2 have lower ΔG_f^{Va} than CeO_2. Then, by calculating ΔG_{max}, it was found that Cr_2CO_2 and V_2CO_2 are the two most active catalysts with the values of ΔG_{max} being −0.2 eV (step II) and 0.26 eV (step I), respectively, as illustrated in Fig. S5.† Except Cr_2CO_2 and V_2CO_2, the other M_2CO_2 compounds have relatively low intrinsic COOR catalytic activity *via* the M–vK mechanism. For example, when used as a substrate of COOR catalysts, the surface oxygen atoms of Ti_2CO_2 [6] are not involved in the elementary reactions and thus the COOR occurs on Ti_2CO_2-based catalysts *via* the L–H or E–R mechanism rather than the M–vK mechanism. Therefore, our findings are applicable to the case for M_2CO_2, which once

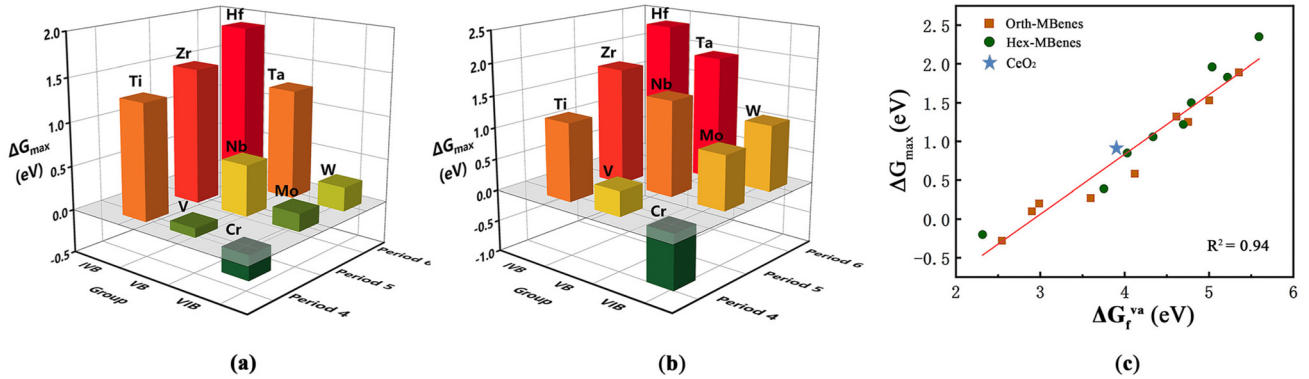

Fig. 5 ΔG_{max} for COOR of (a) orth-$M_2B_2O_2$ and (b) hex-$M_2B_2O_2$ with M in different groups and periods. (c) Relationship between ΔG_{max} and ΔG_f^{Va} of orth/hex-$M_2B_2O_2$.

again supports the conclusion that ΔG_f^{Va} can serve as the descriptor for COOR catalytic activity.

Conclusions

By investigating the COOR catalytic activity of 18 $M_2B_2O_2$ with first-principles methods, hex-$Mo_2B_2O_2$, orth-$Mo_2B_2O_2$, hex-$V_2B_2O_2$, and hex-$Cr_2B_2O_2$ were found to possess high COOR catalytic activity *via* the M–vK mechanism and high thermal stability under 1000 K. Hex-$Mo_2B_2O_2$ is expected to serve as the substrate of COOR catalysts as an alternative to CeO_2, and orth-$Mo_2B_2O_2$, hex-$V_2B_2O_2$, and hex-$Cr_2B_2O_2$ are expected to be used as direct COOR catalysts with higher activity. Furthermore, it was found that the formation energy of O vacancies (ΔG_f^{Va}) can reflect the value of maximum Gibbs free energy change (ΔG_{max}) for COOR catalysis and serve as the descriptor for COOR catalytic activity. In general, materials with lower ΔG_f^{Va} have lower ΔG_{max}. Thus, during the process of COOR catalyst screening, only ΔG_{max} needs to be calculated, thereby saving large amounts of calculation cost and contributing to high screening efficiency.

Conflicts of interest

There are no conflicts to declare.

Acknowledgements

This work was financially supported by the National Natural Science Foundation of China (no. 51871009 and 51872017).

References

1 S. Jiménez, J. Soler, R. X. Valenzuela and L. Daza, *J. Power Sources*, 2005, **151**, 69–73.
2 J. J. Baschuk and X. Li, *Int. J. Energy Res.*, 2001, **25**, 695–713.
3 H. J. Kim, M. G. Jang, D. Shin and J. W. Han, *ChemCatChem*, 2020, **12**, 11–26.
4 B. K. Min and C. M. Friend, *Chem. Rev.*, 2007, **107**, 2709–2724.
5 B. Qiao, A. Wang, X. Yang, L. F. Allard, Z. Jiang, Y. Cui, J. Liu, J. Li and T. Zhang, *Nat. Chem.*, 2011, **3**, 634–641.
6 X. Zhang, J. Lei, D. Wu, X. Zhao, Y. Jing and Z. Zhou, *J. Mater. Chem. A*, 2016, **4**, 4871–4876.
7 Y. Li, Z. Zhou, G. Yu, W. Chen and Z. Chen, *J. Phys. Chem. C*, 2010, **114**, 6250–6254.
8 G. Spezzati, A. D. Benavidez, A. T. DeLaRiva, Y. Su, J. P. Hofmann, S. Asahina, E. J. Olivier, J. H. Neethling, J. T. Miller, A. K. Datye and E. J. M. Hensen, *Appl. Catal., B*, 2019, **243**, 36–46.
9 P. Schlexer, D. Widmann, R. J. Behm and G. Pacchioni, *ACS Catal.*, 2018, **8**, 6513–6525.
10 C. Cheng, X. Zhang, Z. Yang and Z. Zhou, *ACS Appl. Mater. Interfaces*, 2018, **10**, 32903–32912.
11 Z. Jiang, P. Wang, X. Jiang and J. Zhao, *Nanoscale Horiz.*, 2018, **3**, 335–341.
12 F. Li, Y. Li, X. C. Zeng and Z. Chen, *ACS Catal.*, 2015, **5**, 544–552.
13 Y. Lou, Y. Cai, W. Hu, L. Wang, Q. Dai, W. Zhan, Y. Guo, P. Hu, X.-M. Cao, J. Liu and Y. Guo, *ACS Catal.*, 2020, **10**, 6094–6101.
14 Y.-Q. Su, I. A. W. Filot, J.-X. Liu and E. J. M. Hensen, *ACS Catal.*, 2018, **8**, 75–80.
15 X.-m. Zhang, P. Tian, W. Tu, Z. Zhang, J. Xu and Y.-F. Han, *ACS Catal.*, 2018, **8**, 5261–5275.
16 C. Cheng, X. Zhang, Z. Yang and K. Hermansson, *Adv. Theory Simul.*, 2019, **2**, 1900006.
17 S. Y. Hwang, E. Yurchekfrodl, C. Zhang and Z. Peng, *ChemCatChem*, 2016, **8**, 97–101.
18 X. Zhang, C. Xu, Y. Zhang, C. Cheng, Z. Yang and K. Hermansson, *Int. J. Hydrogen Energy*, 2021, **46**, 8477–8485.
19 J.-X. Liu, Y. Su, I. A. W. Filot and E. J. M. Hensen, *J. Am. Chem. Soc.*, 2018, **140**, 4580–4587.
20 M. Moses-DeBusk, M. Yoon, L. F. Allard, D. R. Mullins, Z. Wu, X. Yang, G. Veith, G. M. Stocks and C. K. Narula, *J. Am. Chem. Soc.*, 2013, **135**, 12634–12645.

21 A. J. Therrien, A. J. R. Hensley, M. D. Marcinkowski, R. Zhang, F. R. Lucci, B. Coughlin, A. C. Schilling, J.-S. McEwen and E. C. H. Sykes, *Nat. Catal.*, 2018, **1**, 192–198.
22 E. J. Peterson, A. T. DeLaRiva, S. Lin, R. S. Johnson, H. Guo, J. T. Miller, J. Hun Kwak, C. H. F. Peden, B. Kiefer, L. F. Allard, F. H. Ribeiro and A. K. Datye, *Nat. Commun.*, 2014, **5**, 4885.
23 C. Cheng, X. Zhang, M. Wang, S. Wang and Z. Yang, *Phys. Chem. Chem. Phys.*, 2018, **20**, 3504–3513.
24 Y.-L. Song, L.-L. Yin, J. Zhang, P. Hu, X.-Q. Gong and G. Lu, *Surf. Sci.*, 2013, **618**, 140–147.
25 G. Glaspell, H. M. A. Hassan, A. Elzatahry, V. Abdalsayed and M. S. El-Shall, *Top. Catal.*, 2008, **47**, 22–31.
26 Y. Feng, Q. Wan, H. Xiong, S. Zhou, X. Chen, X. I. Pereira Hernandez, Y. Wang, S. Lin, A. K. Datye and H. Guo, *J. Phys. Chem. C*, 2018, **122**, 22460–22468.
27 H. A. Tahini, X. Tan and S. C. Smith, *ChemCatChem*, 2020, **12**, 1007–1012.
28 M. Naguib, M. Kurtoglu, V. Presser, J. Lu, J. Niu, M. Heon, L. Hultman, Y. Gogotsi and M. W. Barsoum, *Adv. Mater.*, 2011, **23**, 4248–4253.
29 M. Naguib, V. N. Mochalin, M. W. Barsoum and Y. Gogotsi, *Adv. Mater.*, 2014, **26**, 992–1005.
30 Y. Wei, P. Zhang, R. A. Soomro, Q. Zhu and B. Xu, *Adv. Mater.*, 2021, **33**, 2103148.
31 Z. Guo, J. Zhou and Z. Sun, *J. Mater. Chem. A*, 2017, **5**, 23530–23535.
32 B. Zhang, J. Zhou and Z. Sun, *J. Mater. Chem. A*, 2022, **10**, 15865–15880.
33 B. Zhang, J. Zhou, Z. Guo, Q. Peng and Z. Sun, *Appl. Surf. Sci.*, 2020, **500**, 144248.
34 T. Zhang, B. Zhang, Q. Peng, J. Zhou and Z. Sun, *J. Mater. Chem. A*, 2021, **9**, 433–441.
35 B. Li, Y. Wu, N. Li, X. Chen, X. Zeng, Arramel, X. Zhao and J. Jiang, *ACS Appl. Mater. Interfaces*, 2020, **12**, 9261–9267.
36 F. Li and Q. Tang, *ACS Appl. Nano Mater.*, 2019, **2**, 7220–7229.
37 E. Wang, B. Zhang, J. Zhou and Z. Sun, *Appl. Surf. Sci.*, 2022, **604**, 154522.
38 X. Guo, S. Lin, J. Gu, S. Zhang, Z. Chen and S. Huang, *Adv. Funct. Mater.*, 2021, **31**, 2008056.
39 Y. Xiao, C. Shen and T. Long, *Chem. Mater.*, 2021, **33**, 4023–4034.
40 X. Yang, C. Shang, S. Zhou and J. Zhao, *Nanoscale Horiz.*, 2020, **5**, 1106–1115.
41 X. Liu, Z. Liu and H. Deng, *J. Phys. Chem. C*, 2021, **125**, 19183–19189.
42 Y. Xiao, C. Shen and N. Hadaeghi, *J. Phys. Chem. Lett.*, 2021, **12**, 6370–6382.
43 M. Yao, Z. Shi, P. Zhang, W.-J. Ong, J. Jiang, W.-Y. Ching and N. Li, *ACS Appl. Nano Mater.*, 2020, **3**, 9870–9879.
44 S. Xing, J. Zhou, B. Zhang and Z. Sun, *J. Phys. Chem. C*, 2022, **126**, 14275–14282.
45 G. Kresse and J. Furthmüller, *Comput. Mater. Sci.*, 1996, **6**, 15–50.
46 G. Kresse and J. Furthmüller, *Phys. Rev. B: Condens. Matter Mater. Phys.*, 1996, **54**, 11169–11186.
47 G. Kresse and D. Joubert, *Phys. Rev. B: Condens. Matter Mater. Phys.*, 1999, **59**, 1758–1775.
48 J. P. Perdew and Y. Wang, *Phys. Rev. B: Condens. Matter Mater. Phys.*, 1992, **45**, 13244–13249.
49 J. P. Perdew, K. Burke and M. Ernzerhof, *Phys. Rev. Lett.*, 1996, **77**, 3865–3868.
50 S. Nosé, *J. Chem. Phys.*, 1984, **81**, 511–519.
51 S. Qi, Y. Fan, L. Zhao, W. Li and M. Zhao, *Appl. Surf. Sci.*, 2021, **536**, 147742.
52 T. Bo, P.-F. Liu, J. Xu, J. Zhang, Y. Chen, O. Eriksson, F. Wang and B.-T. Wang, *Phys. Chem. Chem. Phys.*, 2018, **20**, 22168–22178.
53 N. Miao, J. Wang, Y. Gong, J. Wu, H. Niu, S. Wang, K. Li, A. R. Oganov, T. Tada and H. Hosono, *Chem. Mater.*, 2020, **32**, 6947–6957.
54 K. Rasoul, K. Mohammad, W. Vei, M. Nanxi, S. Chen, W. Jianfeng and W. Junjie, *J. Phys.: Condens. Matter*, 2020, **33**, 155503.
55 M. Zafari, A. S. Nissimagoudar, M. Umer, G. Lee and K. S. Kim, *J. Mater. Chem. A*, 2021, **9**, 9203–9213.
56 J. Zhou, J. Palisaitis, J. Halim, M. Dahlqvist, Q. Tao, I. Persson, L. Hultman, P. O. Å. Persson and J. Rosen, *Science*, 2021, **373**, 801–805.
57 J. Wang, T.-N. Ye, Y. Gong, J. Wu, N. Miao, T. Tada and H. Hosono, *Nat. Commun.*, 2019, **10**, 2284.
58 T. Hu, M. Wang, X. Wang, Y. Zhou and C. Li, *Comput. Mater. Sci.*, 2021, **199**, 110810.
59 B. Anasori, M. R. Lukatskaya and Y. Gogotsi, *Nat. Rev. Mater.*, 2017, **2**, 16098.
60 W. Sun, S. A. Shah, Y. Chen, Z. Tan, H. Gao, T. Habib, M. Radovic and M. J. Green, *J. Mater. Chem. A*, 2017, **5**, 21663–21668.